




# Fabrication and performance analysis of set standard natural dye-sensitized solar cell (N-DSSC) using extracted *Terminalia kattapa* (Red), *Azadirachia indica* (Green), and *Clitoria ternatea* (Blue) dyes with virgin Degussa p25 photo-anode

T. G. Vignesh Prabhu<sup>1</sup>, J. Chandrasekaran<sup>1,\*</sup>, D. Thangaraju<sup>2</sup> , P. Vivek<sup>1</sup>, and S. Gopi<sup>1</sup>

<sup>1</sup>Department of Physics, Sri Ramakrishna Mission Vidyalaya College of Arts and Science, Coimbatore, Tamil Nadu 641020, India

<sup>2</sup>nano-crystal Design and Application Lab (n-DAL), Department of Physics, PSG Institute of Technology and Applied Research, Coimbatore, Tamil Nadu 641062, India

Received: 6 April 2022

Accepted: 15 June 2022

Published online:  
29 June 2022

© The Author(s), under exclusive licence to Springer Science+Business Media, LLC, part of Springer Nature 2022

## ABSTRACT

Three different natural dyes, such as *Terminalia kattapa* (Red, fruit), *Azadirachia indica* (Green, leaf), and *Clitoria ternatea* (Blue, flower), were extracted to fabricate natural dye-sensitized solar cell (N-DSSC) with standard TiO<sub>2</sub> nanoparticles (p25) on the FTO base layer. A comparative study was carried out on the performance of RA, GA, and BA-based DSSCs based on optical and electrical properties. The anatase and rutile phases on bare TiO<sub>2</sub> film have been confirmed along with the formation of titanium sub-oxides due to the annealing process confirmed by X-ray diffraction. Significant absorption in the visible region has been attained in photo-anodes, which was confirmed with an optical band gap reported from UV reflectance spectra. For the proper electron injection process, a specific functional group has been identified in extracted sensitizer using Fourier transform infrared spectra to ensure the adsorption capability of dye molecules toward TiO<sub>2</sub> particles. Photocatalytic properties of photo-anode have been analyzed using photoluminescence (PL) spectra by investigating the rate of recombination via PL intensity. J-V characteristics of fabricated N-DSSC with extracted natural dyes show that the N-DSSC with GA photo-anode offered the highest efficiency (0.79%) among other dyes used in this investigation, such as RA (0.51%) and BA-based photo-anode (0.29%). DSSCs fabricated using photo-anodes RA, GA, and BA (using water as solvent) show excellent outstanding stability and decent efficiency than the ethanol-based cells.

Address correspondence to E-mail: jchandaravind@yahoo.com

## 1 Introduction

One of the fastest-growing technology in renewable energy is the fabrication of eco-friendly low-cost solar cells. The photovoltaic research community has been extensively united in proliferating the efficiency of photovoltaic devices; as a result, the spotlight falls in the field of emergence DSSCs for their promising photovoltaic conversion capability and economic viability [1]. Also, DSSC can be the best alternative concept for junction photovoltaic devices because it comes up both technically and economically trustworthy [2]. The dye-sensitized solar cell can be fabricated by sensitizing dye on a broader band-gap semiconductor so that it acts as a photo-anode for converting the light energy into electric current in an efficient way [3]. Metal–oxide–semiconductors show wide band gap such as ZnO, SnO<sub>2</sub>, and TiO<sub>2</sub>, which can utilize solar spectrum. TiO<sub>2</sub> is considered the most promising inorganic semiconductors acceptor material in DSSCs fabrication among all other metal oxides. This material possesses many favorable aspects, such as high dielectric constant ( $\epsilon = 80$ ), high refractive index ( $n = 2.5$ ), high band gap (3.2 eV), chemical stability, and high packing density. Particularly, TiO<sub>2</sub> photo-anode favors natural pigments for adsorption so that it shows an effective match in CB and LUMO energy levels between photo-anode and sensitizer. Such a match is essential for attaining effective electron injection [4]. The cost of the sensitizer dyes in practice throws challenges in the fabrication of low-cost DSSC, which leads to the search for low-cost sensitizer pigments.

In general, an ideal sensitizer should show intense absorption in the visible range, attenuated optical energy gap, a prolonged excited lifetime for electrons, narrow band gap between HOMO and LUMO, and faster dye molecule adsorption on semiconductor oxides with favorable anchorage [5]. The function of the dye here is to harvest photons that energize the electron via excitation and inject them into the conduction band (CB) of the semiconductor. Meanwhile, the redox couple in the electrolyte regenerates the dye molecule by recollecting its lost electron from the counter electrode. Hence, the cycle of light to electricity conversion is completed via recollecting. The ruthenium polypyridyl complex was used for higher efficiency because it possesses highly efficient metal-to-ligand charge transfer and intense absorption in the visible region [6]. Despite its advantage,

ruthenium metals are retrieved from long-term rare natural resources that are heavy and resemble to pronounce environmental impediments; and undergo a complex manufacturing process [7, 8]. Easy extracted natural dye sensitizer can be used instead of high-cost ruthenium-based dye for maintaining low cost [9]. Around 150 types of plants are the source of natural dye sensitizers with a wide range of colors. The main criteria for achieving good efficiency in the natural dye system are to select a sensitizer that shows the absorption spectrum is in the visible to the near-infrared region [10]. Eco-friendly dyes derived from natural sources such as anthocyanins, chlorophyll, carotene, and tannin [11] have been explored as natural dye sensitizers.

Among natural eco-friendly dyes, tannin is constructed from the elements such as C, H, and O (often large molecules were formed), resulting in a mixture of a complex polyphenolic compound. Tannin extracted from naturally occurring plants source is a water-soluble polyphenolic compound (containing phenolic hydroxyl groups that, in turn, enable a crosslink between other macromolecules and proteins). *Terminalia catappa* grows in the tropical areas of India and contains dye compounds such as flavonoids and rich tannins. Also, *Terminalia catappa* skin releases tannic acids and has approximately six phenolic acid compounds while extracting dye. In addition, tannins were classified into two types based on their chemical structure and nature: hydrolyzed tannins and condensed tannins. Hydrolyzed tannin is a yellow-brown compound, hygroscopic and amorphous, which is soluble in the polar organic solvent but insoluble in the non-polar organic solvent. [12]. Likewise, *Clitoria ternatea* is an ornamental plant that usually grows in neutral soil. The deep-blue color of the flower is a result of the high content of ternatins (polyacrylate derivatives of delphinidin 3,3',5'-trigluconide), which is one among them from the large varieties of anthocyanins [13]. This flower also includes large varieties of chemical compounds such as anthocyanins, triterpenoids, steroids, and flavonol glycosides [14]. On the other hand, Crude extract of *Azadirachia indica* leaves has revealed the presence of flavonoids, saponins, alkaloids, tannins, amino acids, and steroids [15, 16]. All three raw natural samples possess rich-coloring pigment and can be used as a photo-sensitizer for effective light harvesting.

In this work, *Terminalia kattapa* (Red fruit; R), *Azadirachia indica* (Green leaf; G), and *Clitoria ternatea*

(Blue flower; B) were extracted using water as the solvent for long-lasting purposes: as a photo-sensitizer to sensitize the bare photo-anode. Bare photo-anode has been coated with P25-TiO<sub>2</sub> metal oxides using the doctor blade method. Counter electrode (CE) has been fabricated using carbon as a catalyst. Liquid electrolytes without additives were prepared using potassium iodide (KI), iodine, and acetonitrile. The parts of N-DSSCs, such as photo-anode and CE, were assembled using blinder clips cascaded with iodide electrolyte. Also, the overall efficiency of N-DSSCs was evaluated by J-V performance: using the photovoltaic parameters, which were calculated and discussed in detailed.

## 2 Materials and methods

### 2.1 Preparation of natural dye

Three cells were fabricated in this work using dye extract of *Terminalia catappa* fruit outer peel (RA), *Azadirachia indica* leaves (GA), and *Clitoria ternatea* flower (BA) anchored TiO<sub>2</sub> as a photo-anode.

To extract these sensitizers, 50 g of each material, such as the outer peel of *Terminalia catappa* fruit, leaf of *Azadirachta indica*, and flowers of *Clitoria ternatea*, were taken separately. That was soaked in 150 ml of water for 10 days under dark conditions at pH 3.0 by adding HCl acid [17]; the acid content prevents fungi production [18–21]. Ethanol-based natural dye extraction produced higher efficiency, diminishing results after exposure to sunlight [22]. Water is chosen as extracting solvent for increasing the stability of natural dye. Then the shocking solution is centrifuged and filtered with the Whatman filter paper to remove solid residues, as shown in Fig. 1. The sensitizer is obtained further using a 0.20 μm single-use syringe filter and stored at 4 °C [23].

### 2.2 Preparation of photo-anode

Titanium (IV) oxide (p25) powder of 20 nm primary particle size was purchased from ALDRICH and was used for a bare-photo-anode fabrication. Fluorine-doped oxide (FTO) substrate was used as the transparent conducting substrate (TCO) that acts as a base layer for photo-anode and counter electrode fabrication. FTO substrate was washed with acetone and ethanol separately for 15 min in an ultrasonic bath.

Then, this cleaned FTO substrate is then masked (by scotch tape) on the rest of the film by exposing the active layer to be coated (with an area of 1 cm<sup>2</sup> on the conducting side). The TiO<sub>2</sub> sol-gel paste was prepared by stirring 0.1 g of p25 in 10 drops of concentrated HNO<sub>3</sub> and 20 drops of acetic acid with a rice pellet. Using the Doctor-blade technique, the masked FTO substrate was coated with p25 paste and allowed to dry for a few minutes. After removing the polymer mask, films were subjected to 450 °C for 30 min to get rid of internal gases and voids and then allowed to cool down slowly to room temperature (to avoid cracking or resulting in the breakage of the film). The sensitizing process is done by immersing the bare p25 photo-anode into the filtrated dye solution for 24 h under dark conditions for effective dye loading [24, 25]. Properly air-dried dye-anchored photo-anode was used for further DSSC construction.

### 2.3 Preparation of counter electrode

A new FTO substrate was taken to prepare the counter electrode (CE) in which conducting surface is coated with carbon using 6 HB pencils and a candle flame. After which, this carbon-coated counter electrode was annealed at 450 °C for 30 min and allowed to cool slowly for long-lasting purposes. Then it was washed with ethanol and allowed to dry gently to remove unreacted surface carbon. Hence, this carbon-coated CE is used as a catalyst for enhancing efficiency [26].

### 2.4 Preparation of electrolyte

In general, liquid electrolytes consist of three major components such as solvent, ionic conductor, and additives. In this work, iodide electrolyte solution was prepared by mixing 0.83 g (0.5 M) potassium iodide (KI) with 0.127 g (0.05) iodine in acetonitrile (AN) using a rice pellet for 30 min without using additives [27]. The more pronounced effect of additive on the photo-anode suppresses the efficiency of DSSC [28]. The electrolyte is responsible for the inner charge transport between photo-anode to counter electrodes and dye regeneration [29]. It has a significant role in determining photocurrent density ( $J_{sc}$  can be affected by charge transport of redox couple), photo-voltage ( $V_{oc}$  can be affected by redox potential of electrolyte), and fill factor (FF can be affected by diffusion of charge carriers in electrolytes). It directly

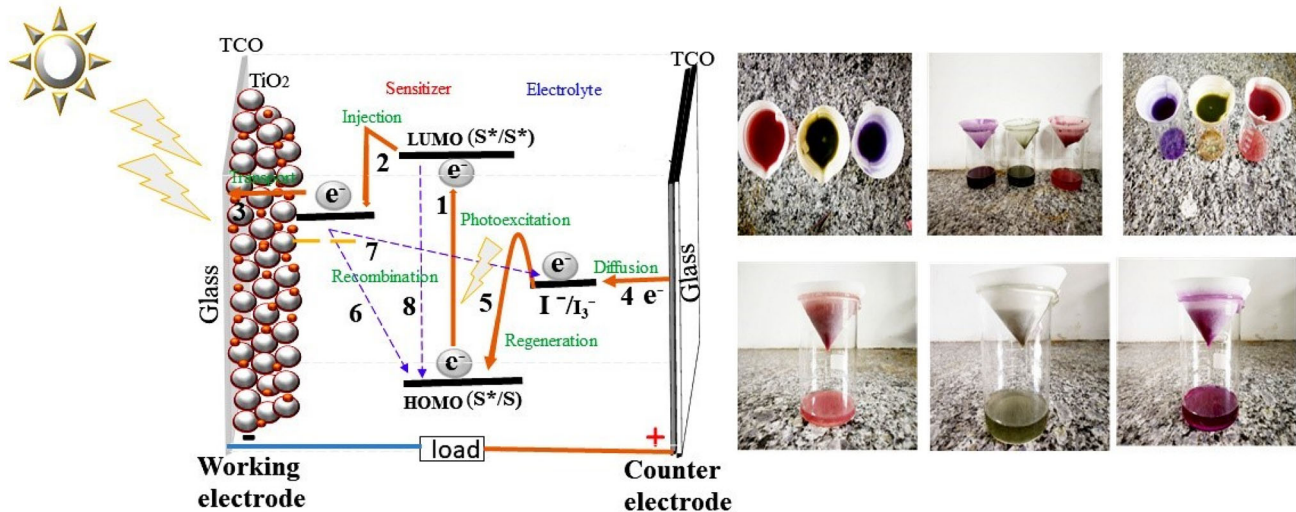


**Fig. 1** Schematic diagram of DSSC cycle and extracted dye from *Terminalia catappa* (Red outer fruit peel), *Azadirachia indica* (Green leaves), and *Clitoria ternatea* (Blue flower)

impacts the light-to-electric conversion efficiency and device stability [30].

## 2.5 Assembling DSSC

The dye-sensitized solar cell was assembled by fixing a p25-based photo-anode cast with liquid electrolyte and CE. The photo-anode sensitized with dye will be facing down onto the CE. It should be slightly offset to connect with the crocodile clips as an output terminal. Further, two electrodes were pressed against the electrolyte by placing them at the edges of the film. The electrolyte was drawn in between the electrodes-spaced capillary action.

## 2.6 Characterization and measurement

Crystal structure and size were calculated using a PANalytical X'pert PRO powder X-ray diffractometer. Optical and physical phenomena were calculated using a V-770 JASCO UV-VIS-NIR spectrophotometer. Quantitative analysis of the various chemical groups was calculated using FP8300 JASCO FTIR spectrometer. The material's electronic structure (imperfection and impurities) and electron lifetime were analyzed by FP8300 spectrofluorometer. The overall efficiency of the assembled cell was determined (defined as the ratio of the maximum output divided by the power of the incident light) using KEITHLY 6517B electrometer with Pecell solar simulator as an input power source.

## 3 Result and discussion

### 3.1 Powder X-ray diffraction

The XRD patterns of p25 film at 450 °C are shown in Fig. 2. In general, Degussa p25 is a mixed phase of anatase/rutile (Degussa p25) [31]. Therefore, the peak position and relative intensities are in accordance with standard powder diffraction patterns. Meanwhile, titanium oxides lost their oxygen and formed their sub-oxides ( $Ti_3O_5$  and  $Ti_2O_3$ ) [32] due to the annealing process. Consequently, these sub-oxides improve the adsorption capability, and dense dye coverage can be attained over the bare photo-anode, which leads to effective light harvesting [33]. Due to defect states, these powders show excellent photoresponse under visible irradiation [32].

Two different phases of  $TiO_2$  (anatase and rutile) and their sub-oxides peak were observed in the XRD pattern; these sub-oxides were produced during annealing. The anatase phase of  $TiO_2$  is in good agreement with JCPDS card # 89-4921. It has a preferred peak of 25.3  $2\theta$  corresponding to the orientation plane (101) and other peak positions at 37.8  $2\theta$  (004) and 48.1  $2\theta$  (200). Moreover, the anatase phase of  $TiO_2$  will enhance the cell's efficiency by enhancing the dye adsorption capability [34]. The rutile phase of  $TiO_2$  is matched with JCPDS card # 89-4920. Its prominent peak position at 27.4  $2\theta$  represents the plane of (110), and its other peak position at 54.4  $2\theta$  (211) and 65.6  $2\theta$  (221). As such, titanium sub-oxide:

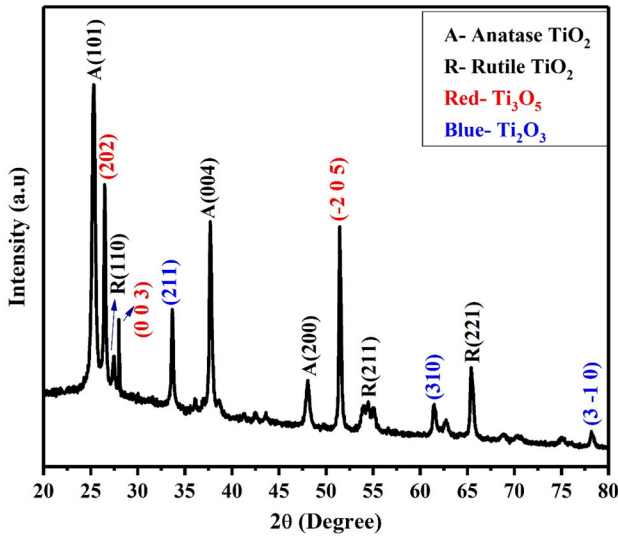


Fig. 2 XRD pattern of TiO<sub>2</sub> (p25) annealed at 450 °C

Ti<sub>2</sub>O<sub>3</sub> corresponding peak values of 33 2θ (211), 61.3 2θ (310), and 78.5 2θ (3-1, 0) are in agreement with the JCPDS card # 85–0868, and in this way, Ti<sub>3</sub>O<sub>5</sub> sub-oxide also shows corresponding peak values of 26 2θ (202), 28.3 2θ (003), and 51.4 2θ (– 205) which are in agreement with the JCPDS card # 82-1138. As a result of defective oxides, photon to electron conversion will increase due to shifting the Fermi level of TiO<sub>2</sub> to a positive direction [35].

Identified sub-oxides (Ti<sub>2</sub>O<sub>3</sub> and Ti<sub>3</sub>O<sub>5</sub>) exhibit different crystal structures such as rhombohedral and monoclinic, respectively. Moreover, anatase and rutile phases of TiO<sub>2</sub> exhibit the same tetragonal crystalline structure. The crystalline size can be calculated using Debye-Scherrer’s equation using XRD data:

$$D = \frac{K \times \lambda}{\beta \times \cos\theta} \tag{1}$$

where *D* is crystal size, *λ* refers to the wavelength of the X-ray radiation (0.15406 nm), *K* is the constant value of 0.9, and *β* is the line width of half maximum height. The average crystalline size obtained using this formula is 25.37 nm.

### 3.2 UV–VIS–NIR spectroscopy

The light absorption capability of TiO<sub>2</sub>-extracted dye samples and dye-anchored photo-anode that was measured with UV–VIS–NIR reflectance spectrum and are compared in Fig. 3. Figure 3a compares the absorption spectra of p25 film at 450 °C with p25

particles. The maximum absorption peak has been blue shifted from 320 nm ( p25 particle) to 270 nm (p25 film at 450 °C) with an increase in absorption [36]. The optical band-gap (*E<sub>g</sub>*) values are estimated for p25 nanoparticles and film by extrapolating straight lines in Tau’s plots using the flowing relation [37–39]:

$$(\alpha hv)n = B(hv - E_g) \tag{2}$$

where *n* = 2 direct transition, *α* is the absorption coefficient, *hν* is the incident photon energy, *B* is the constant, and *E<sub>g</sub>* is the optical band energy. The optical band gap of the p25 particle is determined as 3.2 eV, and for film, it is estimated as 2.6 eV, as shown in Fig. 3b. The absorption peaks of the three extracted dye sensitizers are investigated, as represented in Fig. 3c. The maximum peak absorbed for R, G, and B type dyes are 240 nm, 232 nm, and 212 nm. The other absorption peaks were also identified at 274 nm for R and at 269 nm for G. Three absorption peaks are found at 275 nm, 572 nm, and 613 nm for the B dye sample. Significant absorption in the visible region has been noted after sensitizing this dye on bare p25 film, as shown in Fig. 3e. The electronic energy levels changes within the molecules conjugation with non-bonding electrons, conjugated unsaturation, and the extent of the π-electrons system can be obtained using this spectroscopy technique. For example, the peak at 572 and 613 nm for B sensitizer is indexed by ternatin anthocyanin [22].

After sensitizing dye extract on the bare photo-anode, absorption has increased in the visible region. This is mainly attributed to the dense coverage of the sensitizer [40]. The coverage density of the dye molecule determines the electron loss in the DSSC device. If the bare photo-anode is not adequately covered with dye, then a reaction between injection electron and triiodide ion occurs, which leads back to electron transfer. At the same time, highly loaded films with dye also result in lower efficiency because electron injection decreases due to multilayer adsorption [41].

In this work, the value of band gap has been found in the order of *Azadirachia indica* (G, GA) < *Terminalia kattapa* (R, RA) < *Clitoria ternatea* (B, BA) for both dye extract and respective sensitized photo-anode from DRS spectra as shown in Fig. 3d and f.

RA sample shows two significant peaks at 260 and 312 nm while R dye shows three significant peaks at 204 nm, 274 nm, and 366 nm. The maximum

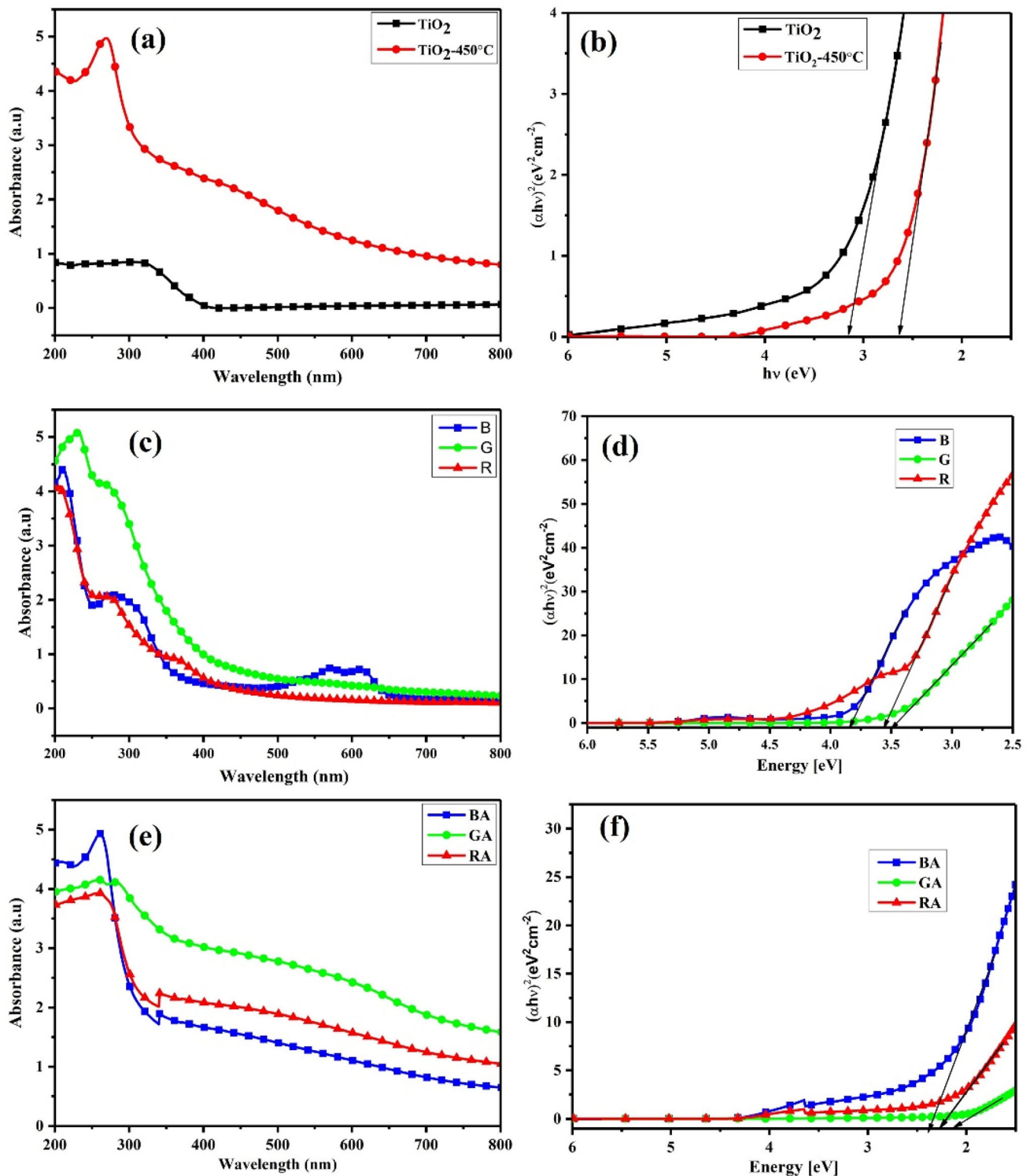


**Fig. 3** Absorption and reflectance spectra of  $\text{TiO}_2$  powder samples (a and b), extracted dyes (c and d), and dye-anchored  $\text{TiO}_2$  layer (e and f)

absorption peak of R has been redshifted from 204 to 260 nm in RA with lower absorption. The optical band gap of R and RA has been determined using

Tau's plots as 4.3 eV and 2.2 eV, respectively. In this way, GA shows two significant peaks at 258 and 284 nm, and raw G has peaks at 232 and 269 nm. The

maximum absorption peak of G has been redshifted from 212 to 259 nm in GA sample. Tau's plots showed a significant band-gap difference between G and GA, 3.8 eV and 2 eV. In the case of BA, it shows two major absorption peaks at 260 and 343 nm and while B has peaks at 210 nm, 275 nm, 572 nm, and 613 nm. The maximum absorption peak of B has been redshifted from 232 to 261 nm in BA. Using Tau's plots, the optical band gap of B and BA has been determined as 3.9 eV and 2.5 eV, respectively. Therefore, from Fig. 3d and f, the optical band gap on the sensitizer is compared with the respective photo-anode in Table 1.

The maximum absorption of all three photo-anode is below 400 nm, which is related to a band gap near 2.6 eV within the TiO<sub>2</sub> nanocrystals due to band-to-band transition [42]. Among them, BA has possessed a maximum absorption peak at 261 nm, followed by RA (260 nm) and GA (259 nm), which shows a broader absorption spectrum in the visible region. This result reveals that the effective light harvest can be established with these three photo-anodes. Especially GA shows the lowest optical band gap of 2 eV followed by RA (2.2 eV) and BA (2.5 eV). This indicates that GA required less energy ( $\Delta E$ ) to transfer an electron from HOMO to LUMO level. Hence, the bare p25 photo-anode band gap shows a good absorption in the visible region after dye loading. Moreover, proper absorption in optical spectra is required to enhance substantial photocurrent in the device. Hence, all three photo-anodes sensitized with except dyes can be effectively used as light harvesting.

### 3.3 FTIR spectroscopy

The adsorption capability of extracted dye toward TiO<sub>2</sub> should be high for effective electron injection from excited sensitizer to TiO<sub>2</sub>. Therefore, dye molecules should possess a specific functional group for effective adsorption toward TiO<sub>2</sub>, which would increase the photon to electron conversion efficiency [43].

The FTIR spectrum was used to identify the functional group of sensitizers R, G, and B, whereby the

compatibility of these dye molecules toward TiO<sub>2</sub> can be estimated. The spectrum of these three sensitizers shows similar peaks, and they are indicated in Fig. 4a–c. Three major broad peaks were found for R at 3314, 2114, and 1636.3 cm<sup>-1</sup>. The same peak pattern was observed for G at 3320.82, 2113, and 1637.2 cm<sup>-1</sup>, whereas in the case of B, three significant peaks were found at 3301.5 cm<sup>-1</sup>, 2116 cm<sup>-1</sup>, and 1636.03 cm<sup>-1</sup>, along with the additional peak at 2360 cm<sup>-1</sup>.

In general, small peaks in the region 1630–1680 cm<sup>-1</sup> exhibit the stretching vibration of C=O corresponding to the amide class of compound [44, 45]. Therefore, such broader peaks at 1636.3, 1637.2, and 1636.3 cm<sup>-1</sup> seemingly indicate the presence of the C=O stretching vibration of tertiary amides that are possible to be present in the range between 1630 and 1670 cm<sup>-1</sup> [46].

The peaks in region 3600–3200 cm<sup>-1</sup> indicate a dye's -OH, -NH<sub>2</sub>, and NH functional group, which indicates N-H and O-H's vibrating stretching, respectively [47]. Therefore, the broader peaks at 3314.07, 3320.82, and 3301 cm<sup>-1</sup> could be the overlapping of N-H and O-H stretching vibration. Depending on the band's intensity, position, and breadth gives more information of the function group. The absorption frequency values vary depending on the hydrogen bonding strength [48–50].

Likewise, the range between 2100 and 2300 cm<sup>-1</sup> is the region where alkynes, cyanates, isocyanates, and cyanides absorb, especially, between 2100 and 2140 cm<sup>-1</sup>, and the stretching of -C≡C- occurs. Hence, the peaks at 2114, 2113, and 2116 cm<sup>-1</sup> correspond to C≡C [45].

Finally, one additional small peak at 2360 cm<sup>-1</sup> (obtained in B sensitizer) arises due to the interaction of ester with water [51], which results in the indication of O-H stretching [37]. The FTIR spectra peaks of this current work agreed and reported by Keka et al. [37] on blue dye from butterfly pea via microwave-assisted methodology.

**Table 1** The calculated band gap of dyes and dye-anchored TiO<sub>2</sub> layers

Samples	<i>Terminalia kattapa</i>		<i>Azadirachia indica</i>		<i>Clitoria ternatea</i>	
	R	RA	G	GA	B	BA
Optical band gap (eV)	4.3	2.2	3.8	2	3.9	2.5

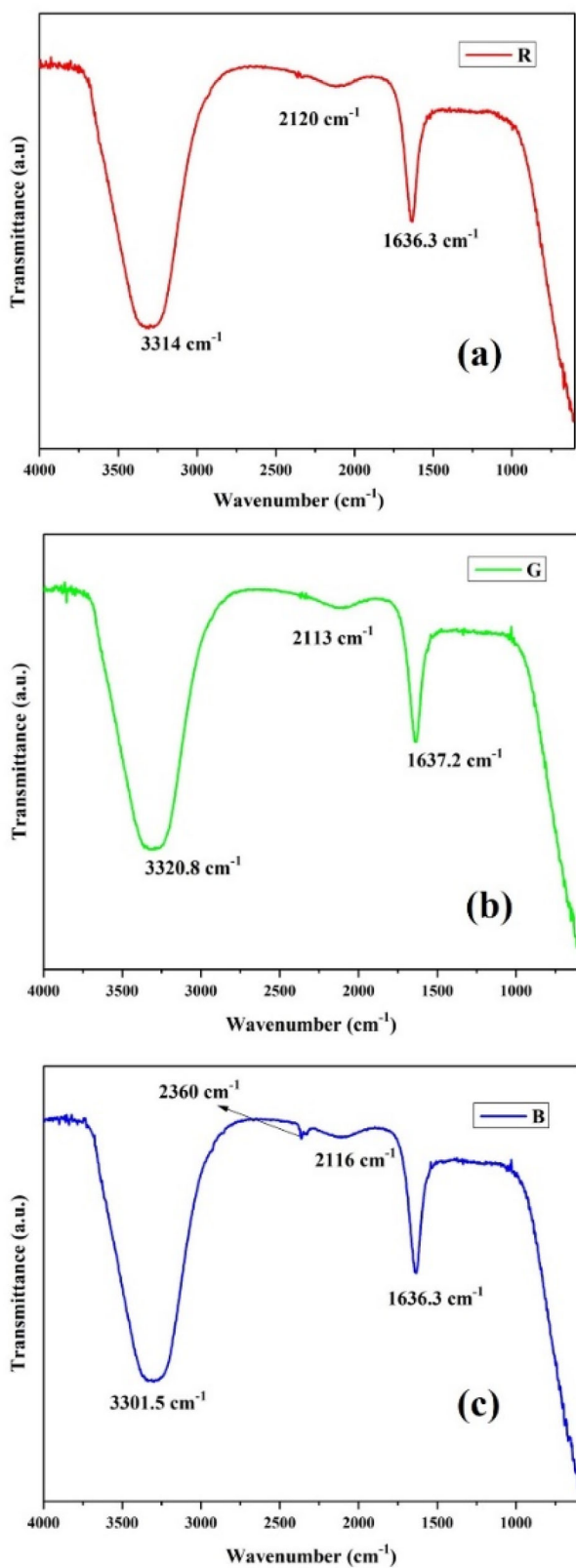


**Fig. 4** FTIR analysis for sensitizer R (a), G (b), and B (c) dyes

FTIR spectral analysis shows a favorable function group, such as OH, C=O, and NH, except dyes molecules that can bond with TiO<sub>2</sub> [52, 53]. It exhibits an adsorption nature toward TiO<sub>2</sub> so that effective electron injection can occur from the excited sensitizer to TiO<sub>2</sub>.

### 3.4 Photoluminescence (PL) studies

This work compares the separation efficiency of photo-generated electrons and holes at room temperature for sensitizer (R, G, and B) with the respective photo-anode (RA, GA, and BA). PL emission of sensitizers R and G was studied using 350 nm excitation wavelength at room temperature, whereas in the case, that of B is at 570 nm, and the recorded spectra are depicted in Fig. 5a–c. Figure 5d illustrates the PL spectrum of three sensitizers, R, G, and B. R and G correspond to the maximum peak at 435.5 and 448 nm and another peak at 530 and 535 nm, respectively, whereas in B, only one prominent peak at 635.5 nm is obtained.

The PL emission of RA, GA, and BA photo-anodes was studied using an excitation wavelength of 220, 190, and 210 nm at room temperature. Figure 5a partially represents the enlarged drawing of the PL spectra of RA from 250 to 500 nm, which show the three peaks at 260, 293, and 470 nm. In this way, Fig. 5b represents the partially enlarged drawing of the PL spectra of GA from 250 to 450 nm, showing the four peaks at 269, 380, 400, and 414 nm. Likewise, Fig. 5c represents the partially enlarged drawing of the PL spectra of BA from 400 to 460 nm, which show the three peaks at 423, 441, and 448.5 nm. For all three photo-anodes, the peaks around 395–450 nm indicate the transition involved in the recombination of electrons because of intrinsic oxygen vacancies (produced as a result of annealing so that trapped levels within the forbidden band-gap TiO<sub>2</sub> take place [28, 54]). Likewise, a peak around the 465 nm indicates the back-electron transport, resulting in a dark current in the device [42]. In mixed phase of TiO<sub>2</sub>, band gap possesses lower defect if rutile content is higher [55].

PL spectra were employed to analyze further characteristics of photo-generated charge carriers in photo-anode, such as migration, recombination of photo-generated carrier trapping, and separation of the electron–hole pairs and charge transfer. In general, lower PL intensity indicates a lower



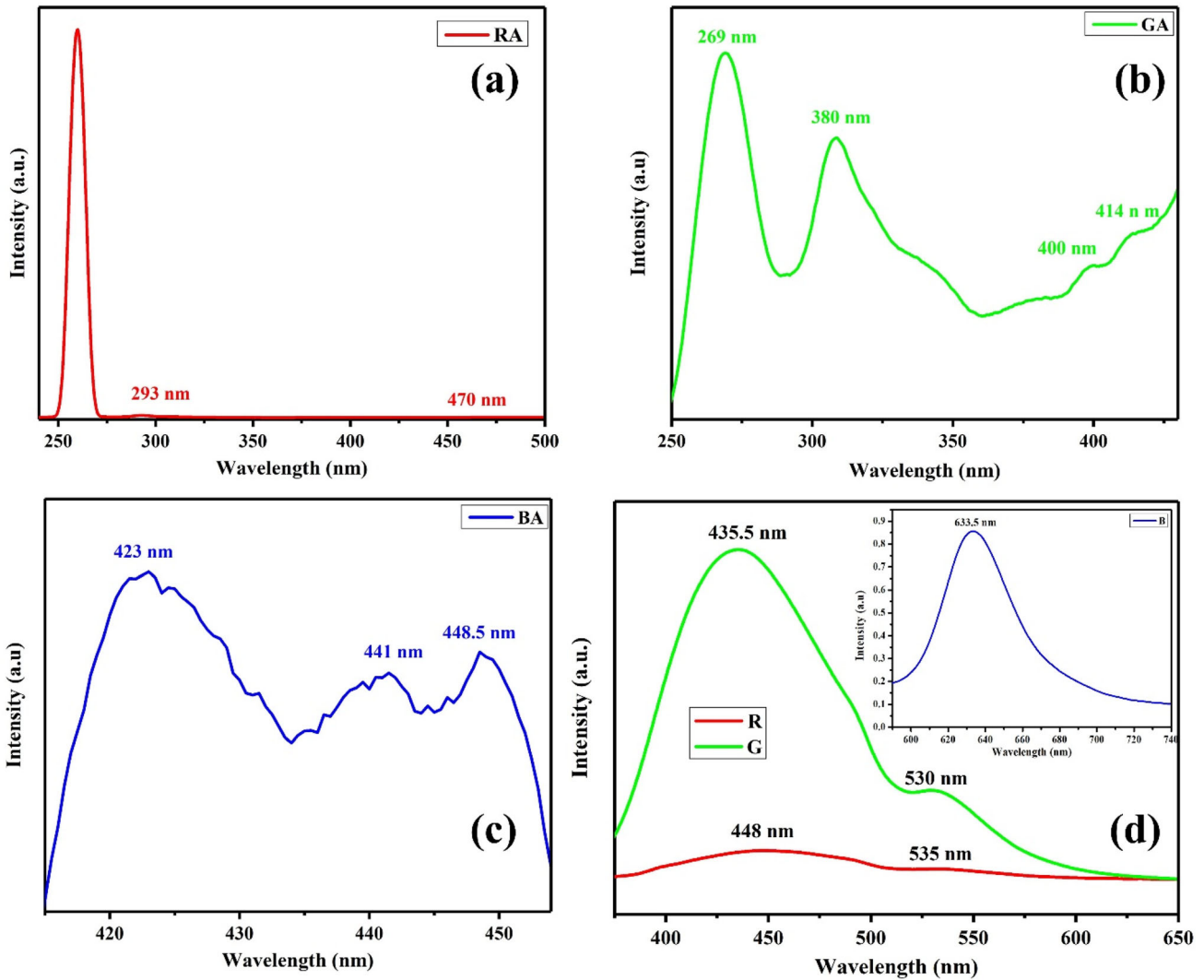


**Fig. 5** Partially enlarged PL spectra of photo-anode for BA (a), GA (b), and RA (c); **d** PL spectra of sensitizer R, G, and B

recombination rate, whereas higher PL intensity indicates a higher charge carrier recombination rate, which could be unfavorable for exhibiting higher photocatalytic properties in photo-anode. The maximum number of free electrons is available (for effective electron charge transport) only when lower PL intensity is obtained, so that effective light harvesting is established by inhibiting recombination. Hence, the PL spectra of all three photo-anodes exhibit lower intensity peaks in the visible region, which could be suitable for exhibiting the excellent photocatalytic property [56]. Hence, all three photo-anode-based N-DSSCs possess higher photocatalytic properties due to the effective generation of electron-hole pairs [57]. Also, the enhanced open-circuit voltage,  $V_{oc}$ , indicates a longer lifetime of the carrier due

to a decrease in PL intensity [58]. Thereby, RA, GA, and BA photo-anodes can assist free electrons for effective light harvesting via enhanced electron-hole separation.

### 3.5 J-V characteristics

Electrical parameters of assembled cells such as fill factor (FF) and overall efficiency ( $\eta$ ) were obtained by substituting the values derived from the J-V graph. Short circuit current ( $J_{sc}$ ), open-circuit current ( $V_{oc}$ ), maximum current density ( $J_{max}$ ), max voltage ( $V_{max}$ ), and intensity of input power ( $P_{in}$ ) were substituted in the following equations [59].

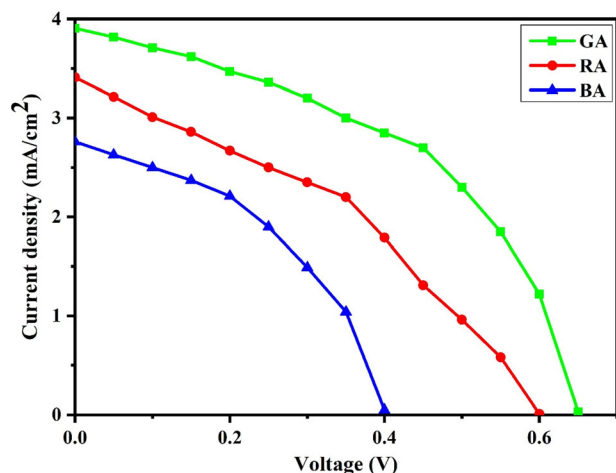


**Fig. 6** J–V characteristic for RA, GA, and BA photo-anode-based DSSCs

$$FF = \frac{J_{\max} \times V_{\max}}{J_{\text{sc}} \times V_{\text{oc}}} \quad (3)$$

$$\eta = \frac{V_{\text{oc}} \times I_{\text{sc}} \times FF}{P_{\text{in}}} \quad (4)$$

J–V characteristics of the three different DSSCs using RA, GA, and BA were obtained via front illumination, as shown in Fig. 6. The electrical parameter for all three cells has been calculated and is listed in Table 2.

From Table 2, it is clear that the  $J_{\text{sc}}$  value of all three cells is in the order of UV absorption spectra. Because there would be a more significant number of dye molecules anchored on the active surface of the photo-anode, which in turn, enhance the transport of electron injection; resulting in an increase in  $J_{\text{sc}}$ , i.e.,

in the order of GA ( $3.9 \text{ mA cm}^{-2}$ ) > RA ( $3.4 \text{ mA cm}^{-2}$ ) > BA ( $2.7 \text{ mA cm}^{-2}$ ).  $V_{\text{oc}}$  reflects the difference in potential between  $\text{TiO}_2$  (fermi level) and electrolyte (redox potential). Thereby, dye coverage over photo-anode is indirectly proportional to the recombination rate. The recombination rate decreases when dye coverage increases by blocking the reduction site and stoppage of the back-electron transfer, leading to higher  $V_{\text{oc}}$  [60]. Thereby, both  $J_{\text{sc}}$  and  $V_{\text{oc}}$  are significant factors in determining the efficiency of the fabricated cell.

It is observed that short circuit current density ( $J_{\text{sc}}$ ) has increased as absorption increases. The reduction of energy band gap occurs with an increase in absorption [61]. Hence, higher efficiency in DSSC is established by effective electron transfer and enhanced absorption in the device along with higher  $V_{\text{oc}}$ . Table 2 compare the conversion efficiencies and photovoltaic performance of natural dyes (using different solvent) related to this work.

## 4 Conclusions

N-DSSCs were effectively fabricated from the dye extract of *Terminalia kattapa* (Red fruit; R), *Azadirachia indica* (Green leaf; G), and *Clitoria ternatea* (Blue flower; B) using water as solvent. Standard bare-photo-anode: p25- $\text{TiO}_2$  layer was successfully coated on FTO using the Doctor-blade technique and annealed at  $450^\circ\text{C}$ . XRD analysis shows the presence of anatase and rutile phases of  $\text{TiO}_2$  with sub-oxides ( $\text{Ti}_3\text{O}_5$  and  $\text{Ti}_2\text{O}_3$ ) as well as the average crystalline size has been estimated as 25.37 nm. After sensitizing

**Table 2** Electrical parameter of fabricated N-DSSC and performance comparison with references (bold values represent current work)

Dye	Sample name (in this work)	Solvent used for dye extract	Metal oxide	JSC ( $\text{mA/cm}^2$ )	VOC (V)	FF	$\eta$ (%)	Reference
<i>Terminalia kattapa</i> (fruit)	<b>RA-DSSC</b>	Ethanol	ZnO	4.9	0.472	0.683	1.58	[11]
		<b>Water</b>	<b>P25</b>	<b>3.4</b>	<b>0.60</b>	<b>0.377</b>	<b>0.51</b>	<b>In this work</b>
<i>Azadirachia indica</i> (leaf)	<b>GA-DSSC</b>	Ethanol	$\text{TiO}_2$	15.10	538	34.6	2.81	[62]
		<b>Water</b>	<b>P25</b>	<b>3.9</b>	<b>0.65</b>	<b>0.470</b>	<b>0.79</b>	<b>In this work</b>
<i>Clitoria ternatea</i> (blue flower)	<b>BA-DSSC</b>	Ethanol	$\text{TiO}_2$	0.203	0.501	0.678	0.069	[63]
		Ethanol	$\text{TiO}_2$	0.481	0.539	0.700	0.182	[63]
		<b>Water</b>	<b>P25</b>	<b>2.7</b>	<b>0.40</b>	<b>0.398</b>	<b>0.29</b>	<b>In this work</b>

with dye extract, the absorption of bare photo-anode has been increased, and it was revealed by the reduction of the optical band gap in all three photo-anodes RA, GA, and BA. UV-Vis spectra reveal that all three photo-anodes show significant absorption in UV and visible regions; significantly broader absorption has been obtained in visible regions. FTIR spectra reveal the presence of a favorable functional group, such as OH, C=O, and NH, so that, except for dyes, molecules (R, G, and B) can bond with TiO<sub>2</sub>. Photocatalytic properties of all three photo-anode possess good photocatalytic properties because of lower PL intensity; enhanced Voc has been established. The J-V characteristics of N-DSSC fabricated using GA as photo-anode show more efficiency (0.79%) than that of RA (0.51%) and BA (0.29%)-based N-DSSCs.

### Author contributions

All the authors contributed to the study conception and design. Materials preparation, data collection, and analysis were performed by TGVP, JC, DT, PV, and SG. All authors read and approved the final manuscript. TGVP: Writing—original draft, JC: Methodology, Conceptualization, Visualization, Methodology, Supervision, Writing—review & editing. DT: Conceptualization, Visualization, Writing—review & editing. PV: Writing—review & editing. SG: Writing—review & editing.

### Funding

This work is not funded by any project.

### Data availability

Data will be made available on reasonable request.

### Declarations

**Conflict of interest** There is no conflict of interest, and, if accepted, the article will not be published elsewhere in the same form, in any language, without the publisher's written consent.

### References

1. G. Calogero, G. Di Marco, S. Caramori, S. Cazzanti, R. Argazzi, C.A. Bignozzi, *Energy Environ. Sci.* **2**, 1162 (2009)
2. E. Middleton, C. Kandaswami, T.C. Theoharides, *Pharmacol. Rev.* **52**, 673 (2000)
3. M.E. Yeoh, K.Y. Chan, *Int. J. Energy Res.* **41**, 2446 (2017)
4. J.H. Yang, C.W. Bark, K.H. Kim, H.W. Choi, *Materials* **7**, 3522 (2014)
5. M.R. Narayan, *Renew. Sustain. Energy Rev.* **16**, 208 (2012)
6. S. Hao, J. Wu, Y. Huang, J. Lin, *Sol. Energy* **80**, 209 (2006)
7. L. Reijnders, *J. Clean. Prod.* **18**, 307 (2010)
8. Y. Amao, T. Komori, *Biosens. Bioelectron.* **19**, 843 (2004)
9. J.D.S.D. Souza, L.O.M.D. Andrade, A.V. Müller, A.S. Polo, *Nano Energy* **2**, 69 (2018)
10. L. Giribabu, R.K. Kanaparthi, *Curr. Sci.* **104**, 847 (2013)
11. P.N. Kumar, K. Sakthivel, *Adv. chem. sci.* **12**, 5809 (2017)
12. M. Dikshit, R.K. Samudrasok, *Int. J. Food Sci. Nutr.* **62**, 47 (2011)
13. N. Terahara, M. Oda, T. Matsui, Y. Osajima, N. Saito, K. Toki, T. Honda, *J. Nat. Prod.* **59**, 139 (1996)
14. P.K. Mukherjee, V. Kumar, N.S. Kumar, M. Heinrich, *J. Ethnopharmacol.* **120**, 291 (2008)
15. Z.S.S. Al-Hashemi, M.A. Hossain, *Pac. Sci.* **18**, 128 (2016)
16. S. Kumar, T.W. Kang, S.J. Lee, S. Yuldashev, S. Taneja, S. Banyal, M. Singhal, G. Ghodake, H.C. Jeon, D.Y. Kim, R.K. Choubey, *J. Mater. Sci.* **30**, 6977 (2019)
17. S. Kumar, H.C. Jeon, T.W. Kang, R. Seth, S. Panwar, S.K. Shinde, D.P. Waghmode, R.G. Saratale, R.K. Choubey, *J. Mater. Sci.* **30**, 17747 (2019)
18. I.K. Mohammed, I.K. Uthman, M.N. Muhammad, *Mater. Sci. Appl.* **3**, 281 (2012)
19. K.U. Isah, U. Ahmadu, A. Idris, M.I. Kimpa, U.E. Uno, M.M. Ndamitso, N. Alu, *Mater. Renew. Sustain. Energy* **4**, 39 (2015)
20. T.A. Ruhane, M.T. Islam, M.S. Rahaman, M.M.H. Bhuiyan, J.M. Islam, M.K. Newaz, K.A. Khan, M.A. Khan, *Optik* **149**, 174 (2017)
21. S. Kumar, S. Taneja, S. Banyal, M. Singhal, V. Kumar, S. Sahare, S.L. Lee, R.K. Choubey, *J. Electron. Mater.* **50**, 3986 (2021)
22. K. Wongcharee, V. Meeyoo, S. Chavadej, *Sol. Energy Mater. Sol. Cells.* **91**, 566 (2007)
23. S. Sathyajothi, R. Jayavel, A.C. Dhanemozhi, *Mater. Today* **4**, 668 (2017)
24. A. Kumar, S. Mukherjee, S. Sahare, R.K. Choubey, *Mater. Sci. Semicond. Process.* **122**, 105471 (2021)
25. A. Kumar, D. Pednekar, S. Mukherjee, R.K. Choubey, *J. Mater. Sci.* **31**, 17055 (2020)

26. V.K. Magotra, T.W. Kang, A.T.A. Ahmed, A.I. Inamdar, H. Im, G. Ghodake, R.K. Choubey, V. Kumar, S. Kumar, *Bio-mass Bioenergy* **152**, 106200 (2021)
27. B. O'regan, M. Grätzel, *Nature* **353**, 737 (1991)
28. M.C. Mathpal, P. Kumar, A.K. Tripathi, R. Balasubramaniyan, M.K. Singh, J.S. Chung, A. Agarwal, *New. J. Chem.* **39**, 6522 (2015)
29. L.M. Gonçalves, V. de Zea Bermudez, H.A. Ribeiro, A.M. Mendes, *Energy Environ. Sci.* **1**, 655 (2008)
30. M. Grätzel, *Acc. Chem. Res.* **42**, 1788 (2009)
31. N. Bouanimba, N. Laid, R. Zouaghi, T. Sehili, *Int. J. Chem. React. Eng.* **16**, 4 (2018)
32. EP 2 842, 627 A1, European patent application 04.03.2015, Bulletin 2015/10. Accessed from <https://patentimages.storage.googleapis.com/24/6f/a6/94f1ea88ca3644/EP2842627A1.pdf>
33. J.T. Kim, S.H. Kim, *Sol. Energy Mater. Sol. Cells* **95**, 336 (2011)
34. S.V. Umale, S.N. Tambat, V. Sudhakar, S.M. Sontakke, K. Krishnamoorthy, *Adv. Powder Technol.* **28**, 2859 (2017)
35. Y. Kim, B.J. Yoo, R. Vittal, Y. Lee, N.G. Park, K.J. Kim, *J. Power Sources* **175**, 914 (2008)
36. S.C. Shei, *Adv. Mater. Sci. Eng.* **2013**, 545076 (2013)
37. J. Tauc, R. Grigorovici, A. Vancu, *Phys. Status Solidi B* **15**, 627 (1966)
38. S. Gupta, R.K. Choubey, L.K. Sharma, M.P. Ghosh, M. Kar, S. Mukherjee, *Semicond. Sci. Technol.* **34**, 105006 (2019)
39. S. Kumar, H.C. Jeon, T.W. Kang, R. Singh, J.K. Sharma, R.K. Choubey, *J. Mater. Sci.* **26**, 3939 (2015)
40. R. Katoh, N. Fuke, A. Furube, N. Koide, *Chem. Phys. Lett.* **489**, 202 (2010)
41. A.C. Khazraji, S. Hotchandani, S. Das, P.V. Kamat, *J. Phys. Chem. B* **103**, 4693 (1999)
42. Y.H. Fan, C.Y. Ho, Y.J. Chang, *Scanning.* **2017**, 9152973 (2017)
43. N.A. Ludin, A.A.A. Mahmoud, A.B. Mohamad, A.A.H. Kadhum, K. Sopian, N.S.A. Karim, *Renew. Sustain. Energy Rev.* **31**, 386 (2014)
44. M.A. Al-Alwani, A.B. Mohamad, A.A.H. Kadhum, N.A. Ludin, *Spectrochim. Acta* **138**, 130 (2015)
45. D. Thangaraju, A. Durairajan, D. Balaji, S.M. Babu, Y. Hayakawa, *Mater. Chem. Phys.* **135**, 1115 (2012)
46. K. Venkata Ramiah, V. Venkata Chalapathi, *Proc. Indian Acad. Sci.* **58**, 233 (1963)
47. D. Thangaraju, S. Moorthy Babu, P. Samuel, A. Durairajan, Y. Hayakawa, *J. Sol-Gel Sci. Technol.* **58**, 419 (2011)
48. S. Cotugno, G. Mensitieri, P. Musto, L. Sanguigno, *Macromolecules* **38**, 801 (2005)
49. D. Murphy, M.N. de Pinho, *J. Membr. Sci.* **106**, 245 (1995)
50. P. Musto, G. Ragosta, L. Mascia, *Chem. Mater.* **12**, 1331 (2000)
51. M. Mališová, M. Horňáček, J. Mikulec, P. Hudec, V. Jorík, *Acta Chim. Slov.* **11**, 147 (2018)
52. K. Xu, B. Liu, Y. Ma, J. Du, G. Li, H. Gao, Y. Zhang, Z. Ning, *Molecules* **14**, 3486 (2009)
53. A.M. Ammar, H.S. Mohamed, M.M. Yousef, G.M. Abdel-Hafez, A.S. Hassanien, A.S. Khalil, *J. Nanomater.* **2019**, 10 (2019)
54. H. Dong, Z. Wu, A. El-Shafei, B. Xia, J. Xi, S. Ning, B. Jiao, X. Hou, *J. Mater. Chem.* **3**, 4659 (2015)
55. J. Liqiang, S. Xiaojun, C. Weimin, X. Zili, D. Yaoguo, F. Honggang, *J. Phys. Chem. Solids* **64**, 615 (2003)
56. N. Kaur, A. Mahajan, V. Bhullar, D.P. Singh, V. Saxena, A.K. Debnath, D.K. Aswal, D. Devi, F. Singh, S. Chopra, *RSC Adv.* **9**, 20375 (2019)
57. P.S. Kumar, M. Selvakumar, S.G. Babu, S.K. Jaganathan, S. Karuthapandian, S. Chattopadhyay, *RSC Adv.* **5**, 57493 (2015)
58. N. Yao, J. Huang, K. Fu, X. Deng, M. Ding, S. Zhang, X. Xu, L. Li, *Sci. Rep.* **6**, 1 (2016)
59. T.A. Ruhane, M.T. Islam, M.S. Rahaman, M.M.H. Bhuiyan, J.M. Islam, T.I. Bhuiyan, K.A. Khan, M.A. Khan, *Sustain. Energy Technol. Assess.* **20**, 72 (2017)
60. H. Chang, Y.J. Lo, *Sol Energy* **84**, 1833 (2010)
61. S. Ito, P. Chen, P. Comte, M.K. Nazeeruddin, P. Liska, P. Péchy, M. Grätzel, *Prog. Photovolt.* **15**, 603 (2007)
62. S. Sahare, N. Veldurthi, R. Singh, A.K. Swarnkar, M. Salunkhe, T. Bhave, *Mater. Res. Express* **2**, 105903 (2015)
63. A. Hayat, A.E.E. Putra, N. Amaliyah, S.S. Pandey, *IOP Conf. Ser.* **619**, 012049 (2019)

**Publisher's Note** Springer Nature remains neutral with regard to jurisdictional claims in published maps and institutional affiliations.